

MCPT-Solver: An Monte Carlo Algorithm Solver Using MTJ Devices for Particle Transport Problems

Siqing Fu¹, Lizhou Wu¹, Tiejun Li^{*}, Xuchao Xie^{*}, Chunyuan Zhang¹,
Sheng Ma¹, Jianmin Zhang¹, Yuhan Tang¹, and Jixuan Tang¹

College of Computer Science and Technology, National University of Defense Technology, Changsha, 410073

Monte Carlo particle transport problems play a vital role in scientific computing, but solving them on existing von Neumann architectures suffers from random branching and irregular memory access, causing computing inefficiency due to a fundamental mismatch between stochastic algorithms and deterministic hardware. To bridge this gap, we propose MCPT-Solver, a spin-based hardware true random number generator (TRNG) with tunable output probability enabled by a Bayesian inference network architecture. It is dedicated for efficiently solving stochastic applications including Monte Carlo particle transport problems. First, we leverage the stochastic switching property of spin devices to provide a high-quality entropy source for the TRNG and achieve high generating throughput and process-voltage-temperature tolerance through optimized control logic and write mechanism designs. Next, we propose a hardware Bayesian inference network to enable probability-tunable random number outputs. Finally, we present a system-level simulation framework to evaluate MCPT-Solver. Experimental results show that MCPT-Solver achieves a mean squared error of $7.6e-6$ for solving transport problems while demonstrating a dramatic acceleration effect over general-purpose processors. Additionally, the MCPT-Solver's throughput reaches 185 Mb/s with an area of $27.8 \mu\text{m}^2/\text{bit}$ and energy consumption of 8.6 pJ/bit, making it the first spin-based TRNG that offers both process-voltage-temperature tolerance and adjustable probability.

Index Terms—Monte Carlo, Stochastic Computing, True Random Number Generators, Spintronic Devices.

I. INTRODUCTION

Particle transport theory describes how particles are scattered, absorbed, and transported through a medium, with extensive applications in fields such as particle physics and radiation medicine [1]. The particle transport problems are typically solved using Monte Carlo (MC) simulation methods, which rely on statistical averages derived from tracking numerous particle histories [2], resulting in substantial computational overhead in high-performance computing (HPC) systems. Although some prior works show that the MC algorithm can be accelerated by exploiting hardware accelerators such as GPU [3], the speedup is very limited due to the fact that its inherently stochastic nature requires frequent irregular accesses to cross-section data during the particle tracking process. Under the conventional von Neumann architecture with its instruction-driven control and hierarchical memory system, this stochasticity in memory access patterns inevitably leads to branch misprediction and large memory access latency [4]. This fundamental limitation stems from the inherent mismatch between the probabilistic nature of MC algorithms and the deterministic behavior in the von Neumann architecture [5].

To address this hardware-software mismatch, developing probabilistic computing architectures with hardware-accelerated stochastic sampling attracts significant research attention to accelerate the MC algorithm in a cost-efficient manner [6]. In practical implementations of stochastic sampling, the primary computational overhead comes from ran-

dom number generation and subsequent sampling operations [5]. Consequently, developing efficient methods for random number sampling and distribution generation represents a fundamental challenge in designing specific architectures for particle transport simulations.

Early solutions are dominated by pseudo-random number generators such as linear congruential generators (LCGs) and linear feedback shift registers (LFSRs), which are flawed by predictability issues [7]. Modern true random number generators (TRNGs) are considered superior in generation speed and quality since they directly leverage physical entropies (e.g., ring oscillators, quantum effects, and spin-based technologies). Spin-based devices are particularly promising thanks to their high power efficiency and CMOS compatibility [8]. While many studies have focused on TRNGs based on spintronics for generating uniformly distributed random sequences [9–13], processor-side post-processing and memory access overhead remains inevitable. A recent spin-orbit torque (SOT) based TRNG [14] enables adjustable distributions but overlooks critical process-voltage-temperature (PVT) tolerance, leading to poor robustness for practical applications.

To address the challenge of designing efficient random sampling hardware for accelerating the MC simulation of Particle Transport problems, we propose MCPT-Solver, a spin-based TRNG featuring probability-tunable outputs enabled by a Bayesian inference network. This design generates random sequences that precisely match particle cross-section distributions, thereby accurately modeling particle transport trajectories. Unlike conventional spin-based TRNGs, MCPT-Solver uniquely supports adjustable output distributions while maintaining PVT tolerance. This is enabled by the write driver design, which controls magnetic tunnel junction (MTJ) stochastic switching via bidirectional voltage application. System-level simulations demonstrate that MCPT-Solver achieves a mean

Manuscript received xx; revised xx. This work is supported in part by the NSFC (62304257, 62472435, 62172430), the STIP of Hunan Province 2022RC3065, and the Foundation of PDL 2023-JKWPDL-02, and the Foundation of NUDT (25-ZZCX-JDZ-16).

¹These authors contributed equally to this work (e-mail: {fusiqingnudt, lizhou.wu}@nudt.edu.cn).

^{*}These authors contributed equally to this work as co-corresponding authors (e-mail: {tjli, xiexuchao}@nudt.edu.cn).

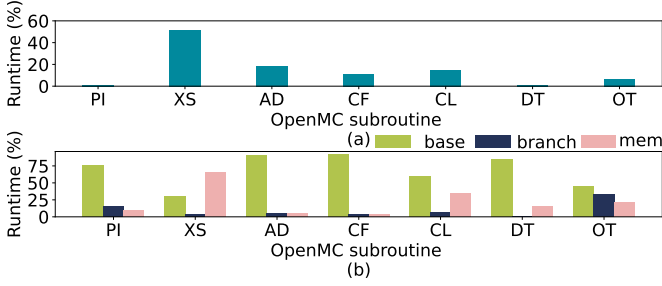


Fig. 1: Performance profiling of Pincell benchmark: (a) subroutine execution time, (b) time breakdown of each subroutine.

squared error (MSE) of 7.6×10^{-6} against the approximate solution in solving particle transport problems, with significant PVT tolerance.

Our main contributions are summarized as follows:

- We introduce a PVT-tolerant TRNG based on spintronic devices with bidirectional write drivers, which maintains robust output distribution under PVT variations.
- We present a Bayesian inference network for generating random numbers with programmable probability distributions, demonstrated by uniform, Gaussian, and problem-specific scattering distributions in this paper.
- We develop a system-level solver which involves co-optimization between spin-based probabilistic hardware simulation and MC particle transport physics modeling.

The remainder of this paper is organized as follows: Section II provides a background for this work. Section III presents the architecture and circuit design of MCPT-Solver. Section IV details the circuit- and system-level performance evaluation. Section V compares MC-Solver with the prior art, and Section VI concludes this paper.

II. BACKGROUND AND MOTIVATION

A. Monte Carlo Simulation for Particle Transport

Particle transport problems arise in diverse engineering fields such as radiation shielding, radiation medicine, and oil well logging. The MC simulation method addresses this type of problems by stochastically sampling particle trajectories through media. The computational workflow consists of three phases: initialization, particle tracking, and tallying. Optimization efforts primarily target the tracking phase due to its high computational demands [15].

We conducted a performance profiling of OpenMC particle transport code [16] using the Pincell benchmark on an Intel Xeon E5-2630 v4 server. Fig. 1(a) shows the run time proportion of OpenMC core subroutines, including particle initialization (PI), cross-section calculation (XS), advancing particles (AD), surface crossing (CF), collision (CL), death (DT), and other (OT) subroutines related to loop control. It can be seen that XS occupies the largest proportion, reaching at 51%. Fig. 1(b) provides a breakdown of each subroutine execution time: base time, branch prediction penalty, and cache miss latency. In XS, cache misses account for 66% of execution time, primarily caused by irregular memory access patterns to cross-section data.

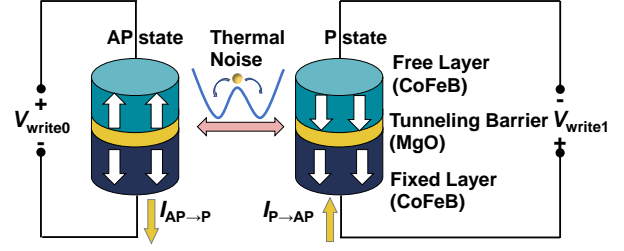


Fig. 2: MTJ structure and stochastic STT switching.

B. Magnetic Tunnel Junction

MTJs have emerged as promising spintronic devices, garnering substantial research attention [13, 17]. The MTJ structure consists of three layers: a pinned layer (PL) with fixed magnetization orientation along the easy axis, a tunnel barrier (TB), and a free layer (FL) whose magnetization can align parallel (P) or antiparallel (AP) to the PL. The high-resistance AP state encodes logic “1”, whereas the low-resistance P state represents logic “0”.

Fig. 2 depicts the stochastic magnetization switching driven by spin-transfer torque (STT) under thermal noise. In the AP state, a spin-polarized current $I_{AP \rightarrow P}$ flows perpendicular to the MTJ, injecting electrons from the PL to the FL. The transferred spin torque induces FL magnetization switching. Similarly, current $I_{P \rightarrow AP}$ triggers reverse switching from P to AP state. With proper current amplitude I_{write} and duration t_{pulse} , the switching becomes stochastic and dominated by dynamic reversal due to thermal fluctuation [12]. The switching probability is given by:

$$P(I_{write}, t_{pulse}) = 1 - \exp\left(-\frac{t_{pulse}}{\tau}\right), \quad (1)$$

$$\tau(I_{write}) = \tau_0 \exp\left[\Delta \left(1 - \frac{I_{write}}{I_{c0}}\right)^2\right],$$

where τ is the average switching time, τ_0 is the attempt time factor, Δ is the thermal stability factor, and I_{c0} is the critical switching current at 0 K. Write voltage V_{write} determines I_{write} , which tunes the switching probability. The thermal noise in MTJ switching provides a quality TRNG entropy for the proposed MCPT-Solver.

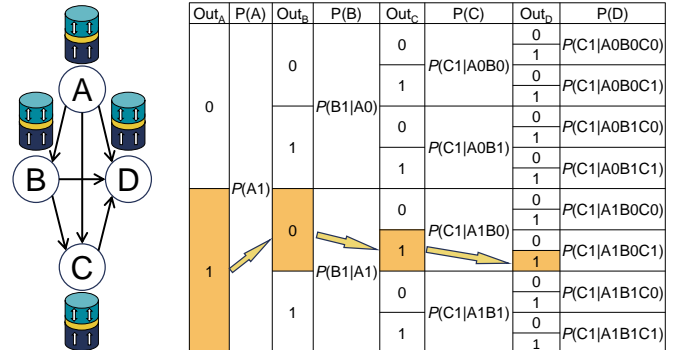


Fig. 3: MTJ-based four-level Bayesian inference network.

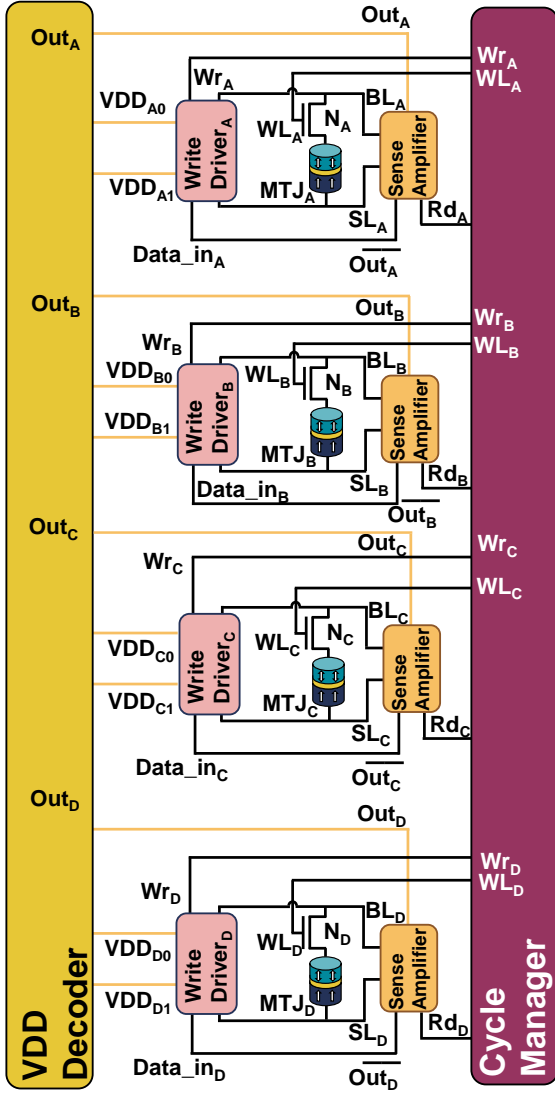


Fig. 4: Circuit design overview of MCPT-Solver.

III. PROPOSED MCPT-SOLVER DESIGN

A. Bayesian Inference Network

MCPT-Solver employs an MTJ-based hardware Bayesian network to generate target probability distributions. The directed acyclic graph (DAG) in Fig. 3 captures the Bayesian network structure, where each node is associated with a conditional probability table (CPT) defining its output probability conditioned on parent states. Directed edges indicate bit-level dependencies that propagate conditional probabilities. Each CPT lists output states (“Out”) and its probability of outputting logic “1”. For example, $P(A1)$ denotes the probability of MTJ_A outputting “1”. Note that $P(A0)$ is omitted in the table as it can be derived with $1 - P(A1)$.

The highlighted CPT path demonstrates an exemplary RNG cycle generating a sequence “1011”. The root node MTJ_A first generates the most significant bit “1” with probability $P(A1)$. Given this output, MTJ_B produces the second bit “0” with probability $1 - P(B1 | A1)$. Next, MTJ_C generates the third bit “1” with probability $P(C1 | A1B0)$. Conditioned

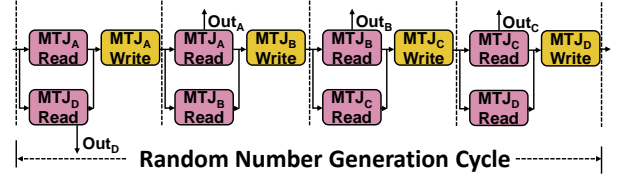


Fig. 5: Control logic of MCPT-Solver.

by the pattern “101”, MTJ_D outputs the fourth bit “1” with probability $P(D1 | A1B0C1)$. According to the Bayesian network chain rule, the joint probability is factorized below:

$$\begin{aligned} P(1011) &= P(A1B0C1D1) \\ &= P(A1) \times (1 - P(B1 | A1)) \\ &\quad \times P(C1 | A1B0) \times P(D1 | A1B0C1). \end{aligned} \quad (2)$$

Other 4-bit random numbers follow a similar probability computation process. Each MTJ requires switching among 1, 2, 4, and 8 conditional probability values respectively. MCPT-Solver selects these values via a VDD decoder, with its circuit design detailed next.

B. Circuit Design Overview

Fig. 4 shows the circuit architecture of MCPT-Solver. The solver consists of multiple Bernoulli Random Number Generators (BRNGs), with four groups shown here, each corresponding to one of the four nodes in the Bayesian network shown in Fig. 3. Each BRNG regulates MTJ switching via bidirectional write voltage applied by the write driver [13]. When PVT variations induce correlated and matched probability shifts in both switching directions, the AP state probability remains invariant. The VDD decoder decodes the higher-bit values to select the corresponding conditional probabilities from the CPT in Fig. 3, enabling hardware-based Bayesian inference. The Cycle Manager coordinates read/write operations using the WL, Rd, and Wr signals.

Fig. 5 illustrates the control logic for generating random numbers: First, Rd_A activates the PCSA sense amplifier [18] to read MTJ_A , then the $\overline{Out_A}$ signal is fed back to $WriteDriver_A$, and the Wr_A signal enables probabilistic writing to MTJ_A . In the second phase, both Rd_A and Rd_B are activated simultaneously to read the states of MTJ_A and MTJ_B . Out_A , as the most significant bit, also drives the VDD decoder to select the voltage pair corresponding to the conditional probability values, namely VDD_{B0} and VDD_{B1} . The write driver then probabilistically writes $\overline{Out_B}$ to MTJ_B , completing the generation of the second bit. Subsequent bits follow an analogous process: simultaneously reading the current and preceding bits, using their combined values via the VDD decoder to select conditional write voltages, and probabilistically updating the MTJ state. The final read operation for MTJ_D overlaps with the next generation cycle.

C. VDD Decoder Design

The VDD decoder in Fig. 6 selects voltage pairs as the voltage inputs for the write driver by decoding the Out

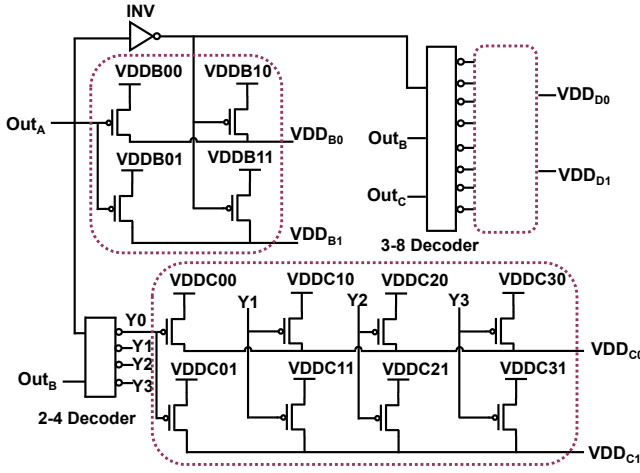


Fig. 6: Structure of the VDD decoder.

TABLE I: Key device parameters for MTJ compact model.

Parameter	Description	Value
t_{FL}	Thickness of the free layer	1.3 nm
$\sigma_{t_{FL}}$	Standard deviation of t_{FL}	3% of 1.3 nm
CD	Critical diameter	32 nm
t_{TB}	Thickness of the tunnel barrier	0.85 nm
$\sigma_{t_{TB}}$	Standard deviation of t_{TB}	3% of 0.85 nm
TMR	TMR ratio	200%
σ_{TMR}	Standard deviation of TMR	3% of 200%

signals from the higher-order BRNG outputs. As the root node, MTJ_A does not require a selection of voltage pairs. For MTJ_B , the decoder selects between two voltage pairs: VDD_{B0} and VDD_{B1} when $Out_A = 0$, VDD_{B10} and VDD_{B11} when $Out_A = 1$, corresponding to $P(B1 | A0)$ and $P(B1 | A1)$, respectively. Voltage pairs follow a hierarchical naming: VDD_{XYZ} , where X is the node, Y is the parent bitmask, and $Z \in \{0, 1\}$ denotes the target state probability. For MTJ_C , the probability of its output being “1” depends on both Out_A and Out_B , and therefore, four pairs of voltage values are available for selection. For instance, when both high-order bits are “0”, after decoding with a 2-4 decoder, $Y0 = 0$, and VDD_{C00} and VDD_{C01} are selected as the write driver inputs. For MTJ_D , there are 8 pairs of voltage values available for selection, with the high three bits used to select through a 3-8 decoder. The PMOS selection structures, similar to those in the previous two stages, are omitted here for clarity.

IV. EXPERIMENTS AND EVALUATION

A. Experimental Setup

SPICE-level simulations employ Cadence Virtuoso with a 45 nm CMOS process (GPDK045), incorporating a compact MTJ model [17]. MC simulations capture MTJ stochastic switching and 3σ process variations, with key parameters in Table I. All simulations, except for those considering temperature variations, were conducted at 27 °C (300 K). The MCPT-Solver system simulator is implemented in Python 3.7 on Ubuntu 20.04.1, using an Intel® Core™i9-12900 CPU.

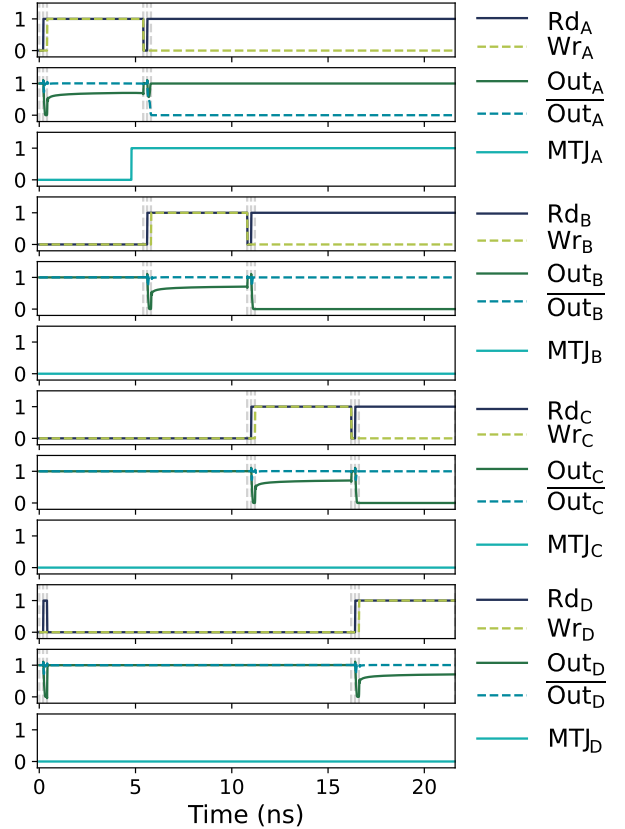


Fig. 7: Sequential timing control and probabilistic switching in MCPT-Solver.

B. Circuit-Level Simulation

1) Random Numbers Generation

Fig. 7 shows the random number generation cycle sequentially processes MTJ_A , MTJ_B , MTJ_C , and MTJ_D , with write probability of each MTJ determined by the state of its higher-order bits, implementing the MTJ-based four-level Bayesian inference network:

- MTJ_A : After a 0.2 ns precharge, the Rd_A signal is enabled, and the current state of MTJ_A (Out_A) is read after 0.2 ns. The inverse value, $\overline{Out_A}$, is then fed back to the input of the write driver $Data_{inA}$. During the 5 ns write window (0.4 ns-5.4 ns), Wr_A enables stochastic switching of MTJ_A . The result is read between 5.4 ns and 5.8 ns, with MTJ_A switching to logic “1” in this simulation.
- MTJ_B : The Rd_B signal is enabled at 5.6 ns, reading the current value of MTJ_B . The voltage pair is selected based on the prior Out_A results. From 5.8 ns to 10.8 ns, the Wr_B signal is enabled, executing a probabilistic write to MTJ_B .
- MTJ_C : The Rd_C signal is enabled at 11 ns, reading the current value of MTJ_C . The voltage pair is selected based on the prior Out_A and Out_B results. From 11.2 ns to 16.2 ns, the Wr_C signal is enabled, executing a probabilistic write to MTJ_C .
- MTJ_D : The Rd_D signal is enabled at 16.4 ns, reading the current value of MTJ_D . The voltage pair is selected

TABLE II: NIST test results for random numbers sequences generated by MCPT-Solver.

Test module		P-value	Pass rate	Pass/Fail
Frequency		0.213309	10/10	Pass
BlockFrequency		0.739918	9/10	Pass
CumulativeSums	Forward	0.213309	10/10	Pass
	Reverse	0.739918	10/10	Pass
Runs		0.534146	10/10	Pass
LongestRun		0.739918	10/10	Pass
Rank		0.739918	10/10	Pass
FFT		0.350485	10/10	Pass
NonOverlappingTemplate		-	1472/1480	Pass
OverlappingTemplate		0.739918	10/10	Pass
ApproximateEntropy		0.350485	10/10	Pass
Serial	Forward	0.017912	10/10	Pass
	Reverse	0.911413	10/10	Pass
LinearComplexity		0.534146	10/10	Pass

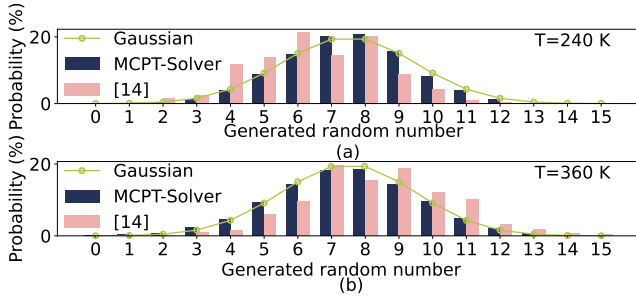


Fig. 8: Comparison of random number distributions generated by MCPT-Solver and the previous method [14] under temperature variations: (a) 240 K, (b) 360 K.

based on the prior Out_A , Out_B and Out_C results. From 16.6 ns to 21.6 ns, the W_{TD} signal is enabled, executing a probabilistic write to MTJ_D . Then the read for MTJ_D overlaps with the first read phase of MTJ_A in the subsequent cycle.

In this cycle, the MCPT-Solver starts in the state “0000” (decimal 0), and generates the result “1000” (decimal 8). By performing MC simulations on the 2^4 possible initial states of the 4-bit sequence and constructing a sequence based on the relationship between previous states and next states, we can obtain the random numbers sequence generated by the MCPT-Solver in the SPICE simulation.

2) NIST Test

Configuring all conditional probabilities to 50% for uniform distribution validation, we evaluate the bit sequences using the NIST Statistical Test Suite. We generated 250,000 random numbers (1 million bits) for the NIST tests, grouped into 10 sets. Table II summarizes the results. The standard threshold is 0.0001, with P-values above this threshold indicating a passing test. As shown, the random bit sequences generated by MCPT-Solver passed all NIST tests, whereas the previous SOT-based design [14] required XOR post-processing, demonstrating the superior quality of MCPT-Solver random numbers generation.

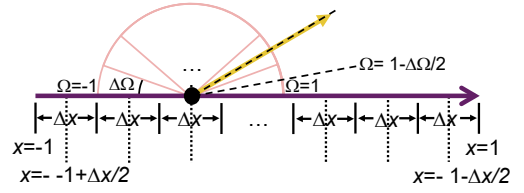


Fig. 9: Spatial particle transport model with $P(t)$ -governed scattering.

3) PVT Tolerance

In this section, we evaluate the PVT variation tolerance of the MCPT-Solver. Since MC simulations inherently account for process variations, we primarily demonstrate the impact of temperature fluctuations on the distribution, while voltage variation effects are comprehensively presented in the system simulation results. Our comparative evaluation replaces the three-terminal SOT-MTJ in [14] with an STT-MTJ, maintaining identical peripheral circuitry for fair comparison.

Both MCPT-Solver and the previous method [14] are configured as discrete Gaussian TRNGs with a mean of 8 and a variance of 4. Fig. 8(a)-(b) illustrate the distribution at ± 60 K relative to room temperature (300 K). The x-axis represents decimal values of 4-bit sequences while the y-axis shows corresponding distribution probabilities. The yellow line indicates ideal distribution, blue bars show MCPT-Solver distribution, and pink bars represent the previous method [14] distribution under same conditions. Under ± 60 K thermal variation, the MCPT-Solver achieves a significantly lower MSE of $3.239e-5$ compared to the $1.077e-3$ MSE of the reference design [14], demonstrating the superior tolerance for temperature variations of our design.

C. System-Level Evaluation

1) Example: Particle Transport Simulations

We consider a particle transport with angular flux density in space, as shown in Fig. 9, where particles undergo scattering events with macroscopic cross-section Σ_s . The particle state space (x, Ω) evolves through Poisson-driven scattering events $P(t)$. Post-scattering directions are sampled from a Gaussian distribution centered on the original direction. The domain $x \in [-1, 1]$ has absorbing boundaries, yielding:

$$\begin{aligned}
 0 &= -v\Omega \frac{\partial}{\partial x} \Phi(x, \Omega) + vR(x) + v\Sigma_s \int (\Phi(x, \Omega + \omega) \\
 &\quad - \Phi(x, \Omega)) p^*(\omega + \Omega | \Omega) d\omega, \\
 x &\in (-1, 1), \quad \Omega \in [-1, 1], \\
 \Phi(1, \Omega) &= 0, \quad \text{if } \Omega < 0, \\
 \Phi(-1, \Omega) &= 0, \quad \text{if } \Omega > 0.
 \end{aligned} \tag{3}$$

We set the particle velocity to $v = 200$ and macroscopic scattering cross-section $\Sigma_s = 0.5$. The spatially-dependent particle source term $R(x)$ is defined piecewise:

$$R(x) = \begin{cases} 0.015 & \text{if } |x| < 0.5 \\ 0 & \text{otherwise.} \end{cases} \tag{4}$$

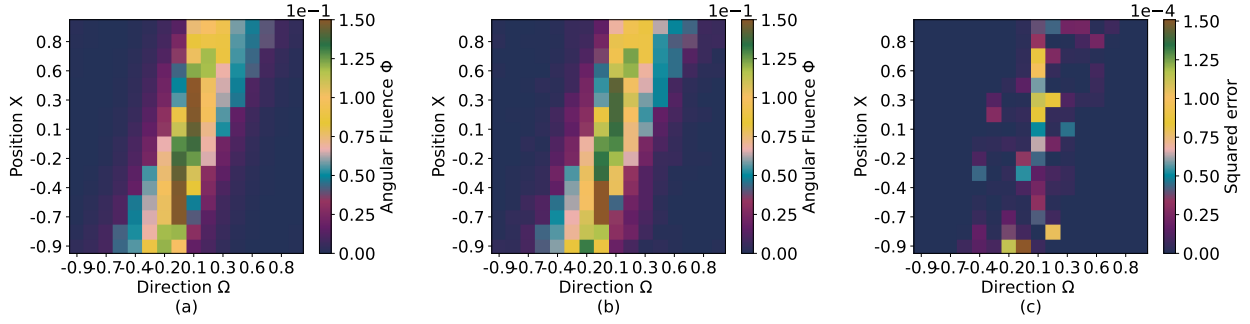


Fig. 10: MC solutions for particle transport: (a) CPU-computed angular flux density (software), (b) MCPT-Solver-computed angular flux density, (c) Squared error comparison.

Scattering events obey Poisson statistics, with angular deflection ω sampled from the Gaussian probability density function:

$$p(\omega) = \frac{1}{\sqrt{2\pi\sigma^2}} \exp\left(-\frac{\omega^2}{2\sigma^2}\right). \quad (5)$$

The analytical intractability of particle transport problem necessitates MC simulation of individual particle trajectories:

$$\begin{aligned} \Phi(x, \Omega) &= \mathbb{E} \left[\int_0^{T_{x,\Omega}} v R(X(u)) du \mid X(0) = x, Y(0) = \Omega \right], \\ dX(t) &= -vY(t) dt, \\ dY(t) &= \omega_{Y(t)} dP(t), \\ T_{x,\Omega} &= \inf \left\{ t > 0 \mid X(t) \notin [-1, 1], \frac{X(0)=x}{Y(0)=\Omega} \right\}. \end{aligned} \quad (6)$$

MC simulations evaluate the expectation in Equation (6) to obtain $\Phi(x, \Omega)$. Particles from the source update direction via $\omega_{Y(t)}$ from Poisson process $P(t)$, with positions updated using velocity v and direction $Y(t)$. Tracking terminates upon exiting $[-1, 1]$, implementing absorption. The solution relies on tracking $\omega_{Y(t)}$.

The MCPT-Solver discretizes the state space into 16 positions and 16 directions, as shown in Fig. 9, with $\Delta x = 1/8$ and positions at interval midpoints:

$$x_i = -1 + \Delta x/2 + (i-1)\Delta x, i \in \{1, \dots, 16\}. \quad (7)$$

The direction space $Y(t) \in [-1, 1]$ is discretized into intervals of size $\Delta\Omega = 1/8$, with each discrete value located at the angular bisectors:

$$\Omega_j = -1 + \Delta\Omega/2 + (j-1)\Delta\Omega, j \in \{1, \dots, 16\}. \quad (8)$$

A Markov model describes particle transitions in Δt . State (i, j) represents position x_i and direction Ω_j , transitioning to (k, l) . The Markov transition matrix $C^* \in \mathbb{R}^{256 \times 256}$, with elements $c_{(i,j) \rightarrow (k,l)}$ encoding all possible state transitions:

$$c_{(i,j) \rightarrow (k,l)} = \begin{cases} 1 - q_1 + q_1 p(0) & \text{if } x_k = x_i - v\Omega_j \Delta t \\ & \text{and } j = l \\ q_1 p(l - j) & \text{if } x_k = x_i - v\Omega_j \Delta t \\ & \text{and } j \neq l \\ 0 & \text{otherwise.} \end{cases} \quad (9)$$

Here, q_1 represents the probability of a Poisson event $P(t)$ occurring once. Finally, we need to define the absorbing state **a**:

$$c_{(i,j) \rightarrow \mathbf{a}} = \begin{cases} 1 & \text{if } |x_i - v\Omega_j \Delta t| > 1 \\ 0 & \text{otherwise.} \end{cases} \quad (10)$$

The complete state transition matrix is:

$$C = \begin{pmatrix} C^* & \mathbf{c}_a \\ 0 & 1 \end{pmatrix}. \quad (11)$$

The transition matrix C encodes transition probabilities, which are queried at every time step Δt during MC simulation of Equation (3). The simulation proceeds in three steps:

- 1) Initialize W particles per state from source $R(x)$.
- 2) Track particles via C until absorption.
- 3) Compute $\Phi(x, \Omega)$ from tracking data following the expectation operator in Equation (6).

In contrast to the uniform scattering assumption in [19], our Gaussian angular kernel better captures realistic scattering physics.

2) Solving Accuracy

The MC simulation process, executed on the CPU, yields the angular flux density solution shown in Fig. 10(a). The x-axis represents particle angle Ω , the y-axis represents particle position x , and the color bar indicates $\Phi(x, \Omega)$, with $W = 10,000$.

We select $W = 100$ to balance accuracy and simulation cost. The MC problem is solved using MCPT-Solver by matching the particle distribution to the distribution defined by the state transition matrix. For a particle in state (i, j) , the next state follows the distribution defined in Equation (9).

The particle tracking process provides the angular flux density solution, shown in Fig. 10(b). The squared error of the solution, with $W = 10,000$ as the approximate solution, is given in Fig. 10(c). The resulting MSE of $7.6e-6$ demonstrates that MCPT-Solver effectively solves the particle transport problem.

3) PVT Tolerance

The tolerance of MCPT-Solver to variations was assessed by applying a $3\sigma = 10\%$ normal distribution perturbation to the MTJ write voltage. The sum of squared errors (SSE) measured 0.00187 for MCPT-Solver compared to 0.00213 for the previous method [14], indicating no significant difference in SSE. These results demonstrate that MC methods inherently

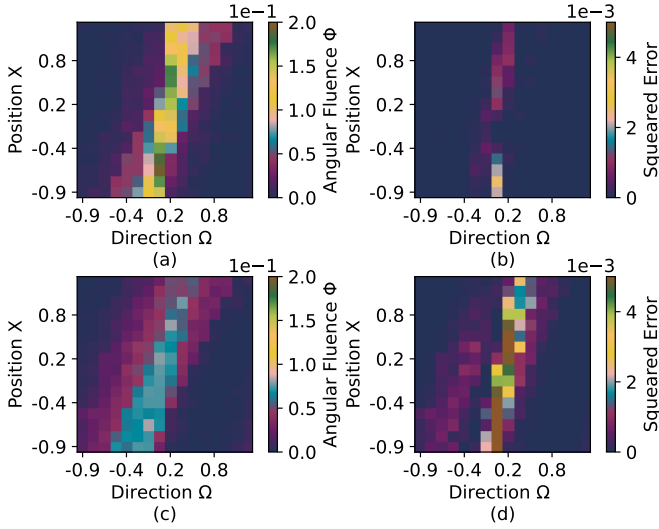


Fig. 11: Accuracy comparison under -15% voltage variations: (a) Solution from MCPT-Solver, (b) Squared error between the MCPT-Solver solution and the approximate solution, (c) Solution from the previous method [14], (d) Squared error between the previous solution and the approximate solution.

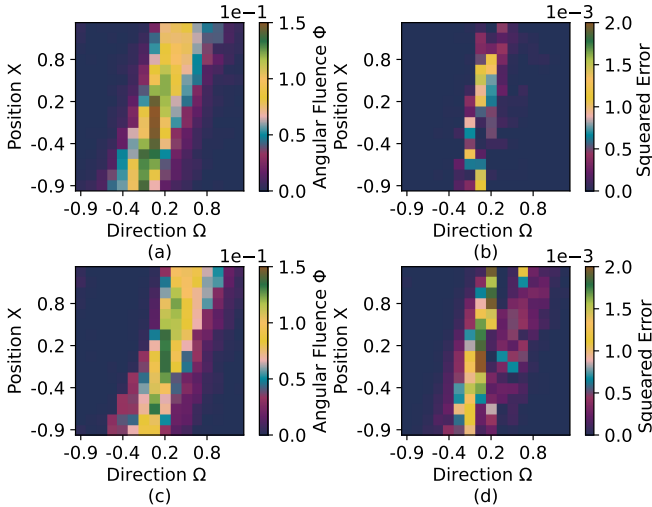


Fig. 12: Accuracy comparison under $+15\%$ voltage variations: (a) Solution from MCPT-Solver, (b) Squared error between the MCPT-Solver solution and the approximate solution, (c) Solution from the previous method [14], (d) Squared error between the previous solution and the approximate solution.

resist normal distribution variations, confirming viability of TRNG as an accelerator for MC simulations.

Besides the normal distribution, we also consider a $\pm 15\%$ voltage variation. Fig. 11(a) shows the angular flux density results from MCPT-Solver under a -15% voltage variation, while Fig. 11(c) shows those from the previous method [14]. The corresponding error analyses appear in Fig. 11(b) for MCPT-Solver and Fig. 11(d) for prior methods. Fig. 12 displays similar results for a $+15\%$ voltage variation. MCPT-Solver consistently shows higher accuracy, as indicated by the error analyses. Table III compares the SSE. The SSE of MCPT-

TABLE III: The SSE of MCPT-Solver and the previous method [14] under $\pm 15\%$ voltage variation.

	-15%	$+15\%$
MCPT-Solver	0.0254	0.0262
[14]	0.1580	0.0651

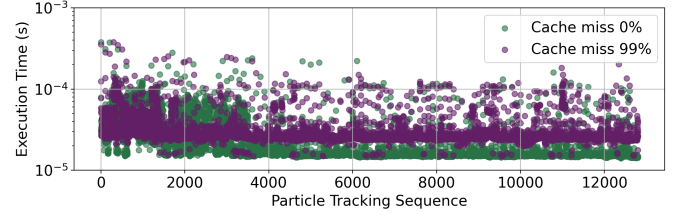


Fig. 13: The CPU time for a single particle tracking includes both low cache miss rate and high cache miss rate as boundary cases.

Solver is only $10\% - 40\%$ of that of the previous method [14], demonstrating its superior resistance to voltage variations.

4) Performance Potential Analysis

To establish a fair comparison with HPC-based MC simulations shown in Fig. 1, model both ideal (0%) and worst-case (99%) cache miss scenarios. Fig. 13 compares CPU execution times per particle for scenarios with 0% and 99% cache misses, with realistic tracking times ranging between $21.954 \mu\text{s}$ and $30.390 \mu\text{s}$ per particle. This serves as a reference for the inefficiencies MCPT-Solver avoids, though actual speedup requires accounting for system-level integration overheads (e.g., I/O, synchronization). The $21.6 \text{ ns}/4\text{-bit}$ generation latency of MCPT-Solver suggests orders-of-magnitude acceleration potential when replacing software-based random sampling, as it eliminates cache misses and unifies probability storage with computation.

It should be noted that the reported acceleration potential metrics is relative to single-CPU-core performance. While previous GPU-based MC methods [20] leverage GPU parallelism to accelerate the entire transport tracking, a GPU with 3584 CUDA cores achieves only a $55.6\times$ speedup compared to a single-core CPU, with single-threaded tracking performance lower than that of the CPU. Thus, we use the single CPU core as the baseline, as it represents the highest-performance unit for particle tracking in a non-parallelized scenario.

V. DISCUSSION

MCPT-Solver demonstrates a 21.60 ns generation cycle for 4-bit random numbers, achieving 185.2 Mb/s bit throughput. Post-layout analysis in GPDK045 technology (Fig. 14) reveals a compact $111 \mu\text{m}^2$ footprint for the four-MTJ-set design. Transient simulations indicate $20.5 \text{ pJ}/4\text{-bits}$ energy consumption, corresponding to 8.6 pJ/bit .

MCPT-Solver outperforms prior spin-based TRNGs [9–13] and recent configurable RNGs [14, 21] in supporting stochastic computing systems, as shown in Table IV. Compared to STT-MTJ-based TRNGs, MCPT-Solver delivers higher throughput than most, except RHS-TRNG [13], due to relaxed write

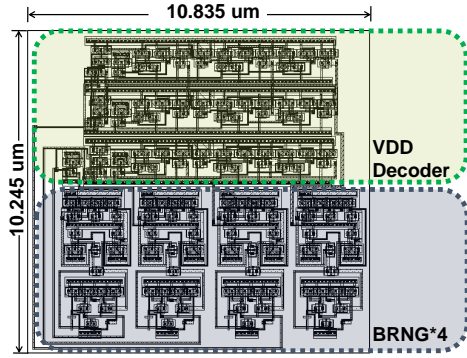


Fig. 14: MCPT-Solver circuit layout.

TABLE IV: Comparison with previous works.

TRNG design	Entropy source	Prob. config. Y/N	True random Y/N	Throughput Mb/s	Power pJ/bit	Area $\mu\text{m}^2/\text{bit}$
[10]	STT-MTJ	N	Y	7.7-15.1	5.7-13.4	50.6-200.6
[9]	STT-MTJ			50	1.1	219
[11]	STT-MTJ			66.7-177.8	0.6-0.8	3.8-7.6
[12]	STT-MTJ			66.7	0.8	3.8
[13]	STT-MTJ			303	2.7-5.3	14.5-24.3
[21]	LFSR	Y	N	1094	8.3e-4	390.8
[14]	SOT-MTJ		Y	< 1000	-	-
MCPT-Solver	STT-MTJ		Y	Y	185.2	8.6

timing for switching probability coverage. Although Tree-GRNG [21] achieves higher throughput, its dependence on pseudo-random LFSR entropy and large $1172.45 \mu\text{m}^2$ area (NAND-normalized: $0.895 \mu\text{m}^2$ [22]) limit its applicability. The SOT-based design [14] lacks area and power details and exhibit lower PVT tolerance than MCPT-Solver, as discussed in Section IV. As the sole PVT-tolerant TRNG combining distribution configurability with true randomness, MCPT-Solver emerges as an ideal accelerator for stochastic computing applications ranging from particle transport to probabilistic machine learning.

Future work will focus on scaling through multi-unit array parallelization and optimizing the host-TRNG interface architecture for efficient hybrid computing. Addressing these challenges will be crucial for translating the theoretical acceleration potential into practical applications.

VI. CONCLUSION

MCPT-Solver harnesses intrinsic STT-MTJ stochasticity as entropy source, implements Bayesian inference via digital VDD decoder, and achieves PVT resilience through write driver optimization. MCPT-Solver simulates particle transport history by generating random sequences that match the particle cross-section distribution. Compared to CPU-based simulations, MCPT-Solver achieves a MSE of $7.6e-6$ by natively embedding transport physics into hardware stochasticity. This approach demonstrates the feasibility of spintronic circuits as accelerators for MC simulation. In comparison to existing spin-based TRNGs, MCPT-Solver uniquely offers adjustable probability distributions and PVT tolerance while maintaining high throughput and acceptable area and power consumption. This study demonstrates the feasibility of spintronic devices as next-generation stochastic accelerators to accelerate scientific computing such as MC simulation of particle transport.

REFERENCES

- [1] R. D. White, R. E. Robson, S. Dujko, P. Nicoletopoulos, and B. Li, "Recent advances in the application of boltzmann equation and fluid equation methods to charged particle transport in non-equilibrium plasmas," *Journal of Physics D: Applied Physics*, vol. 42, no. 19, p. 194001, sep 2009, doi:[10.1088/0022-3727/42/19/194001](https://doi.org/10.1088/0022-3727/42/19/194001).
- [2] A. Haghghat, *Monte Carlo methods for particle transport*. Crc Press, 2020, doi:<https://doi.org/10.1201/9780429198397>.
- [3] S. P. Hamilton, S. R. Slattery, and T. M. Evans, "Multigroup Monte Carlo on GPUs: Comparison of history- and event-based algorithms," *Annals of Nuclear Energy*, vol. 113, pp. 506–518, 2018, doi:[10.1016/j.anucene.2017.11.032](https://doi.org/10.1016/j.anucene.2017.11.032).
- [4] J. Tramm, B. Allen, K. Yoshii, A. Siegel, and L. Wilson, "Efficient algorithms for Monte Carlo particle transport on AI accelerator hardware," *Computer Physics Communications*, vol. 298, p. 109072, 2024, doi:[10.1016/j.cpc.2023.109072](https://doi.org/10.1016/j.cpc.2023.109072).
- [5] S. Misra, L. C. Bland, S. G. Cardwell, J. A. C. Incorvia, C. D. James, A. D. Kent, C. D. Schuman, J. D. Smith, and J. B. Aimone, "Probabilistic neural computing with stochastic devices," *Advanced Materials*, vol. 35, no. 37, p. 2204569, 2023, doi:[10.1002/adma.202204569](https://doi.org/10.1002/adma.202204569).
- [6] M. Alawad and M. Lin, "Survey of stochastic-based computation paradigms," *IEEE TETC*, vol. 7, no. 1, pp. 98–114, 2019, doi:[10.1109/TETC.2016.2598726](https://doi.org/10.1109/TETC.2016.2598726).
- [7] H. Krawczyk, "How to predict congruential generators," *Journal of Algorithms*, vol. 13, no. 4, pp. 527–545, 1992, doi:[10.1016/0196-6774\(92\)90054-G](https://doi.org/10.1016/0196-6774(92)90054-G). [Online]. Available: <https://www.sciencedirect.com/science/article/pii/019667749290054G>
- [8] V. H. González, A. Litvinenko, A. Kumar, R. Khymyn, and J. Åkerman, "Spintronic devices as next-generation computation accelerators," *Current Opinion in Solid State and Materials Science*, vol. 31, p. 101173, 2024, doi:[10.1016/j.cossms.2024.101173](https://doi.org/10.1016/j.cossms.2024.101173).
- [9] A. Amirany, K. Jafari, and M. H. Moaiyeri, "True random number generator for reliable hardware security modules based on a neuromorphic variation-tolerant spintronic structure," *IEEE TNANO*, vol. 19, pp. 784–791, 2020, doi:[10.1109/TNANO.2020.3034818](https://doi.org/10.1109/TNANO.2020.3034818).
- [10] B. Perach *et al.*, "An asynchronous and low-power true random number generator using STT-MTJ," *IEEE TVLSI*, vol. 27, no. 11, pp. 2473–2484, 2019, doi:[10.1109/TVLSI.2019.2927816](https://doi.org/10.1109/TVLSI.2019.2927816).
- [11] Y. Qu, J. Han, B. F. Cockburn, W. Pedrycz, Y. Zhang, and W. Zhao, "A true random number generator based on parallel STT-MTJs," in *IEEE DATE*, 2017, pp. 606–609, doi:[10.23919/DATE.2017.7927058](https://doi.org/10.23919/DATE.2017.7927058).
- [12] Y. Qu, B. F. Cockburn, Z. Huang, H. Cai, Y. Zhang, W. Zhao, and J. Han, "Variation-resilient true random number generators based on multiple STT-MTJs," *IEEE TNANO*, vol. 17, no. 6, pp. 1270–1281, 2018, doi:[10.1109/TNANO.2018.2873970](https://doi.org/10.1109/TNANO.2018.2873970).
- [13] S. Fu, T. Li, C. Zhang, H. Li, S. Ma, J. Zhang, R. Zhang,

- and L. Wu, “RHS-TRNG: A resilient high-speed true random number generator based on STT-MTJ device,” *IEEE TVLSI*, 2023, doi:[10.1109/TVLSI.2023.3298327](https://doi.org/10.1109/TVLSI.2023.3298327).
- [14] R. Zhang, X. Li, M. Zhao, C. Wan, X. Luo, S. Liu, Y. Zhang, Y. Wang, G. Yu, and X. Han, “Probability-distribution-configurable true random number generators based on spin-orbit torque magnetic tunnel junctions,” *Advanced Science*, p. 2402182, 2024, doi:[10.1002/adv.202402182](https://doi.org/10.1002/adv.202402182).
- [15] P. K. Romano, A. R. Siegel, B. Forget, and K. Smith, “Data decomposition of monte carlo particle transport simulations via tally servers,” *Journal of Computational Physics*, vol. 252, pp. 20–36, 2013, doi:[10.1016/j.jcp.2013.06.011](https://doi.org/10.1016/j.jcp.2013.06.011).
- [16] P. K. Romano, N. E. Horelik, B. R. Herman, A. G. Nelson, B. Forget, and K. Smith, “OpenMC: A state-of-the-art Monte Carlo code for research and development,” *Annals of Nuclear Energy*, vol. 82, pp. 90–97, 2015, doi:[10.1016/j.anucene.2014.07.048](https://doi.org/10.1016/j.anucene.2014.07.048).
- [17] L. Wu, S. Rao, M. Taouil, E. J. Marinissen, G. S. Kar, and S. Hamdioui, “MFA-MTJ Model: Magnetic-field-aware compact model of pMTJ for robust STT-MRAM design,” *IEEE TCAD*, vol. 41, no. 11, pp. 4991–5004, 2022, doi:[10.1109/TCAD.2021.3140157](https://doi.org/10.1109/TCAD.2021.3140157).
- [18] W. Zhao, C. Chappert, V. Javerliac, and J.-P. Noziere, “High speed, high stability and low power sensing amplifier for MTJ/CMOS hybrid logic circuits,” *IEEE TMAGN*, vol. 45, no. 10, pp. 3784–3787, 2009, doi:[10.1109/TMAG.2009.2024325](https://doi.org/10.1109/TMAG.2009.2024325).
- [19] J. D. Smith, A. J. Hill, L. E. Reeder, B. C. Franke, R. B. Lehoucq, O. Parekh, W. Severa, and J. B. Aimore, “Neuromorphic scaling advantages for energy-efficient random walk computations,” *Nature Electronics*, vol. 5, no. 2, pp. 102–112, 2022, doi:[10.1038/s41928-021-00705-7](https://doi.org/10.1038/s41928-021-00705-7).
- [20] P. Song, Z. Zhang, L. Liang, Q. Zhang, and Q. Zhao, “Implementation and performance analysis of the massively parallel method of characteristics based on GPU,” *Annals of Nuclear Energy*, vol. 131, pp. 257–272, 2019, doi:[10.1016/j.anucene.2019.02.026](https://doi.org/10.1016/j.anucene.2019.02.026).
- [21] J. Crols, G. Paim, S. Zhao, and M. Verhelst, “TreeGRNG: Binary tree gaussian random number generator for efficient probabilistic AI hardware,” in *IEEE DATE*. IEEE, 2024, pp. 1–6, doi:[10.23919/DATE58400.2024.10546516](https://doi.org/10.23919/DATE58400.2024.10546516).
- [22] Y. Q. Aguiar, F. Wrobel, J.-L. Autran, P. Leroux, F. Saigné, A. D. Touboul, and V. Pouget, “Impact of complex logic cell layout on the single-event transient sensitivity,” *IEEE TNS*, vol. 66, no. 7, pp. 1465–1472, 2019, doi:[10.1109/TNS.2019.2918077](https://doi.org/10.1109/TNS.2019.2918077).



Siqing Fu received the B.Sc. and the M.Eng. degrees in computer science and technology from the National University of Defense Technology (NUDT), Changsha, China in 2018 and 2021, respectively. He is currently pursuing the Ph.D. degree with the College of Computer Science and Technology, NUDT, advised by Prof. T.J. Li.

His research work focuses on non-volatile memory circuit and domain-specific architecture design and optimization.



Lizhou Wu (Member, IEEE) received the B.Sc. degree in electronic science and engineering from Nanjing University, Nanjing, China, the M.Eng. degree in computer science and technology from NUDT, Changsha, China, and the Ph.D. degree (Hons.) in computer engineering from Delft University of Technology.

He is currently an assistant professor at the College of Computer Science and Technology, NUDT. His research interests include: 1) Spintronic design, automation and test, 2) Emerging computing

paradigms based on non-volatile memory devices, 3) Domain-specific computing systems.

Dr. Wu owns five patents and has authored 20+ IEEE/ACM conference (e.g., ITC, DATE, ETS, VTS) and journal (e.g., TCAD, TC, TETC, TVLSI) papers. He has received many international awards such as IEEE TTTC’s E.J. McCluskey Doctoral Thesis Award 2021, Best Paper Award at DATE’20, and three best paper nominations.



Tiejun Li received the B.Sc. and Ph.D. degrees in computer science and technology from the NUDT. He is currently a chair professor with the College of Computer Science and Technology, NUDT. He is the Director of a series of research projects. His research interests include high performance computing and microprocessor architecture.



Xuechao Xie received the PhD degree in computer science from the National University of Defense Technology (NUDT), China, in 2018. Currently he is an assistant professor with the College of Computer, NUDT, China. His current research interests include high performance computing, file and storage systems with non-volatile memory, solid-state drives, and shingled magnetic recording drives.



Chunyuan Zhang (Member, IEEE) received the B.Sc., M.Eng., and Ph.D. degrees in computer science and technology from the NUDT, Changsha, China, in 1985, 1990, and 1996, respectively. He is currently a professor with the College of Computer Science and Technology, NUDT. He is also the director of a series of research projects, including National Natural Science Foundation projects of China. His research interests include computer architecture, parallel programming, embedded systems, and scientific computing.



Sheng Ma received the B.Sc. and Ph.D. degrees in computer science and technology from the NUDT in 2007 and 2012, respectively. He visited the University of Toronto from September 2010 to September 2012 as a co-supervised PhD student. He is currently a professor with NUDT. From December 2012 to December 2021, he successively served as an assistant professor and an associate professor at NUDT. His research interests include microprocessor architecture, AI accelerators, and on-chip networks.



Yuhan Tang received the B.E. degrees in communication engineering from the Hunan Institute of Science and Technology, Yueyang, China. He is currently pursuing the Ph.D. degree with the College of Computer Science and Technology, National University of Defense Technology, Changsha, China. His research work focuses on domain-specific architecture design and optimization. His research interests include high performance computing and microprocessor architecture.



Jianmin Zhang received the B.Sc., M.Eng., and Ph.D. degrees in computer science from the NUDT, Changsha, Hunan, China, in 2001, 2003, and 2008, respectively. He is currently an associate professor in computer science at NUDT.

His major research fields of interest include high performance computer architecture, and interconnect network.



Jixuan Tang Jixuan Tang received the B.E. degrees in Integrated Circuit Design and Integrated System from the NUDT. He is currently pursuing the Ph.D. degree with the College of Computer Science and Technology, NUDT, Changsha, China. His research focuses on analog compute-in-memory architecture and domain-specific-architecture design and optimization.